NeuroImage 56 (2011) 197–211

Contents lists available at ScienceDirect

NeuroImage

journal homepage: www.elsevier.com/locate/ynimg

Smoothness-guided 3-D reconstruction of 2-D histological images

Amalia Cifor [a,*], Li Bai [b], Alain Pitiot [c]

[a] IBME, University of Oxford, Oxford, UK
[b] School of Computer Science, University of Nottingham, Nottingham, UK
[c] School of Psychology, University of Nottingham, Nottingham, UK

ARTICLE INFO

Article history:
Received 2 December 2010
Accepted 20 January 2011
Available online 28 January 2011

Keywords:
Histology
Reconstruction
Curvature flow

ABSTRACT

This paper tackles two problems: (1) the reconstruction of 3-D volumes from 2-D post-mortem slices (e.g., histology, autoradiography, immunohistochemistry) in the absence of external reference, and (2) the quantitative evaluation of the 3-D reconstruction. We note that the quality of a reconstructed volume is usually assessed by considering the smoothness of some reconstructed structures of interest (e.g., the gray–white matter surfaces in brain images). Here we propose to use smoothness as a means to drive the reconstruction process itself. From a pair-wise rigid reconstruction of the 2-D slices, we first extract the boundaries of structures of interest. Those are then smoothed with a min–max curvature flow confined to the 2-D planes in which the slices lie. Finally, for each slice, we estimate a linear or flexible transformation from the sparse displacement field computed from the flow, which we apply to the original 2-D slices to obtain a smooth volume. In addition, we present a co-occurrence matrix-based technique to quantify the smoothness of reconstructed volumes. We discuss and validate the application of both our reconstruction approach and the smoothness measure on synthetic examples as well as real histological data.

© 2011 Elsevier Inc. All rights reserved.

Introduction

Even though 2-D post-mortem imaging technologies (histology, immunohistochemistry, autoradiography etc., hereafter referred to as "histology") continue to outperform classical 3-D imaging technologies (e.g., magnetic resonance imaging) in terms of spatial resolution, contrast and specificity, the qualitative and, crucially, quantitative analysis of the acquired images is still somewhat limited. Because the organs or structures of interest are inherently 3-D objects, the analysis of their shape, the computation of their volume, or the comparison of their characteristics across individuals cannot be accurately performed on the basis of 2-D slices alone. Therefore, 3-D volume reconstruction from the 2-D input slices usually constitutes a first step in the morphological analysis of the structures imaged by serial section histology (Braumann et al., 2005; Ju et al., 2006; Malandain et al., 2004; Yelnik et al., 2007).

3-D reconstruction using 2-D/2-D registration of histological images

A common approach to reconstruction consists in registering consecutive pairs of slices with respect to a reference-slice, generally picked around the middle of the stack (Malandain et al., 2004; Ourselin et al., 2001b).

Registration techniques applied to 2-D histological slices may be classified into manual techniques (Deverell et al., 1993), fiducial markers-based (Breen et al., 2005; Goldszal et al., 1995; 1996; Humm et al., 1995; Toga et al., 1997), features-based (Cohen et al., 1998; Guest et al., 2001; Kim et al., 1995; Zhao et al., 1993) and intensity-based techniques (Kim et al., 1997; Ourselin et al., 2001a).

Manual techniques are usually time-consuming and lack accuracy. The most common procedure for fiducial markers-based methods is to insert extrinsic markers (needle tracks) into the tissue and register the slices by overlying the corresponding needle tracks across the volume. This is an invasive procedure which often damages the histological slices. This issue is bypassed in Refs. (Simonetti et al., 2006; Streicher et al., 1997), where four markers are inserted perpendicular to the chuck onto which the brain tissue is glued and not through the tissue itself. Yet, if the needles are not parallel to the cutting axis, or if the needle holes collapse, this approach may still produce an inaccurate reconstructed volume. In contrast to fiducial markers-based methods, feature-based ones are noninvasive. They consist in automatically extracting features such as points (Guest et al., 2001), edges (Kim et al., 1995) or contours (Cohen et al., 1998; Zhao et al., 1993) from the input slices and using them to guide the 2-D alignment. The accuracy of the reconstruction is then dependent upon the accuracy of the feature extraction step. Finally, iconic (i.e., intensity-based) methods proved very popular for histological images, for instance, Ourselin et al. (2001a) used a robust block-matching algorithm, Kim et al. (1997) proposed a technique which optimizes mutual information, etc.

Note that, a wide range of methods can be used to register two 2-D images. However, the nature and high incidence of the distortions and

* Corresponding author at: Institute of Biomedical Engineering, Department of Engineering Science, Old Road Campus Research Building, University of Oxford, OX3 7DQ, Oxford, UK. Fax: +44 1865 617701.
E-mail address: amalia.cifor@eng.ox.ac.uk (A. Cifor).

1053-8119/$ – see front matter © 2011 Elsevier Inc. All rights reserved.
doi:10.1016/j.neuroimage.2011.01.060

artefacts that occur during the 2-D histological process (shape changes during perfusion, fixation or tissue extraction, holes and tears during cutting, nonlinear shrinking of tissues during preparation, inhomogeneities due to dying etc.) make some approaches unsuitable for 2-D histological slices. For instance, principal axes transformation methods are unable to recover shearing artefacts (Schormann and Zilles, 1997).

What is more, we submit that a 2-D pair-wise registration process is unlikely to yield anatomically satisfactory volumes. Indeed, as argued at length in Ref. (Malandain et al., 2004), the 3-D conformation of the organ or structure is lost during sectioning and cannot be recovered in the absence of external information. By handling only two slices at a time, a typical pair-wise reconstruction method falls prey to a classical aperture problem: registration errors accumulate and propagate throughout reconstruction, compromising the overall shape of the reconstructed volume, which tends to exhibit waving patterns along the cutting axis. This is the humorously nicknamed "the banana problem" (Malandain et al., 2004) also referred to as "z-shift effect" (Yushkevich et al., 2006).

3-D reconstruction using a 3-D reference

The quality of the 3-D volumes reconstructed by the aforementioned techniques may be easily improved when external information about the morphology of the 3-D structures is provided. Such external information is usually supplied by a 3-D imaging modality (e.g., MRI, CT or PET (Mega et al., 1997; Ourselin et al., 2001a; Pitiot et al., 2007; Thompson and Toga, 1996)), or by 2-D block-face images acquired during the sectioning process (Bardinet et al., 2002; Chakravarty et al., 2008; Dauguet et al., 2007; Kim et al., 1997). Those act as an adequate anatomical framework.

Such an approach to fusion is generally twofold. First, a geometrically coherent 3-D volume is reconstructed with a 2-D pair-wise approach. Second, the reconstructed volume is co-registered to the 3-D modality (MR or CT).

For instance, MR/histology fusion was used to validate the analysis of a genotype/phenotype correlation in a recent study of genetically modified rodents (Pitiot et al., 2007). The proposed system took advantage of both the microscopic details offered by histology and the anatomy provided by MRI to describe morphological differences at the macroscopic level linked to genetic alterations. Dauguet et al. (2007) built an initial block-face volume from block-face photographs taken during the cutting process and used it as external reference for the alignment of the histological slices. They attempt to correct deformations in the reverse order of their physical occurrence. A coherent global reconstruction of the histological volume was obtained by registering the 2-D histological slices with the corresponding 2-D block-face slices. In Ref. (Timsari et al., 1999) template sections were used as external references to reduce misalignments.

3-D reconstruction using cross-slice regularization

Nevertheless, an external anatomical reference is not always available or its resolution may be inadequate to guide the 3-D reconstruction process. Therefore, different approaches have been proposed in the literature to alleviate the issues raised by the limitations of the 2-D/2-D pair-wise reconstruction. For instance, the 2-D transformations obtained from the latter can be filtered in the direction across slices (Malandain et al., 2004; Yushkevich et al., 2006), or the classical 2-D pair-wise registration procedure may be extended to a larger neighborhood, such that either a set of slices (Yushkevich et al., 2006) or the whole stack (Guest and Baldock, 1995; Tan et al., 2007; Wirtz et al., 2004) are considered conjointly.

As an illustration, Yushkevich et al. (2006) proposed a graph theoretic technique where each slice was rigidly registered to several neighboring slices instead of just the immediately preceding or following one. This defines a registration graph whose weights are a measure of the quality of those individual registrations. The volume can then be reconstructed by following optimal local paths in the graph. In Ref. (Krinidis et al., 2002), a 3-D histological volume is obtained by optimizing a global energy function of the parameters of the rigid slice transformations. The proposed energy combines the Euclidean distance between each slice and the rigidly transformed slices found in its neighborhood.

In Ref. (Zhao et al., 2004), the authors address the challenge of error accumulation by introducing a new similarity measure. Instead of a pair-wise similarity measure, they use a global alignment one. The intensity values of each image are predicted from the intensity values of the already aligned images found in its neighborhood, along rays parallel to the cutting axis. The global alignment measure consists in quantifying the prediction error which is estimated by a weighted linear regression of the intensity values.

Recent approaches which address the 3-D reconstruction in the absence of external information conjointly manipulate all the slices in the stack. As an illustration, Wirtz et al. (2004) used the global sum of squared differences (SSD) as a similarity measure within the variational framework of the Navier–Lame partial differential system to globally optimize the set of estimated elastic transformations. Tan et al. (2007) proposed to improve upon an initial global reconstruction by estimating affine transformations from three displacement vectors computed between high-curvature points extracted from each slice. These points are extracted from tissue contours after an initial global reconstruction to serve as surrogate fiducial markers. In Ref. (Guest and Baldock, 1995), the histological slices are modeled as thin elastic plates with a smooth reconstruction corresponding to the equilibrium state of a finite element method, which optimizes a distance measure computed with respect to spring forces joining matching points across consecutive slices.

Smoothness-guided reconstruction

We note that the quality of a 3-D reconstruction is usually evaluated by considering the smoothness of some reconstructed structures of interest (the gray–white matter surfaces in a brain for instance), in the direction of the cutting axis (Guest and Baldock, 1995; Ju et al., 2006; Laissue et al., 2008; Tan et al., 2007; Wirtz et al., 2004). For instance, in Ref. (Wirtz et al., 2004), an expert visually examined the smoothness of the borders delimiting anatomical structures of a rat brain histological volume and the amount of small recognizable structures, such as subcortical nuclei and ventricles. Guest and Baldock (1995) quantified the smoothness of the reconstruction based on the assumption that corresponding points across consecutive slices are located close to each other, due to the small thickness of the histological slices and the morphological nature of anatomical structures. Ju et al. (2006) proposed a similar smoothness measurement where corresponding points are determined based on the quality of the 2-D pair-wise matchings computed as an L^2-norm between the warped and reference images. Recently, Laissue et al. (2008) assessed the co-registration errors between MRI and reconstructed histological volume using a distance measure between crest-lines of the lateral ventricles identified in the two brains.

Here, we propose to use smoothness as a means to drive the reconstruction process itself. At a glance, our method uses a constrained min–max curvature flow to smooth the boundaries of structures of interest extracted from an initial rigid reconstruction of the input 2-D histological slices. We make the hypothesis that those slices are sufficiently thin to allow for reconstructed structures to appear smooth in the direction of the cutting axis.

Note that contrary to the technique of Tan et al. (2007), in which a reduced number of displacement vectors are estimated to correct the

slice transformations, we extract an actual displacement field from the flow. This makes it possible to estimate global or local slice transformations from this field, which are then applied independently to the original slices in order to smooth the initial volume.

The proposed smoothing approach also substantially differs from reconstruction techniques based on elastic or nonlinear registration (Gefen et al., 2003; Guest and Baldock, 1995; Schmitt et al., 2007; Thompson and Toga, 1996; Wirtz et al., 2004). Indeed, the min–max curvature flow smooths the boundaries of the structures of interest without making assumptions about the nature of deformations (rigid, linear, elastic etc.). Instead, different types of transformations (linear, nonlinear) can be estimated from the displacement field estimated from the flow, according to the application at hand.

We detail our reconstruction method in the following section and the quantitative approach to the evaluation of volume smoothness in Section 3. We discuss preliminary results on both synthetic and real datasets in Section 4 where we also report on validation data.

Methods

Our technique consists of five steps. (1) First, a classic pair-wise rigid reconstruction is used to build a coherent 3-D volume from the input 2-D slices. (2) Next, boundaries of interest (e.g., the outline of a particular organ, the gray–white matter boundary in cerebral slices) are automatically extracted. (3) We then smooth the extracted 3-D surfaces with a min–max curvature flow confined to the 2-D planes in which the slices lie. (4) From the motion of the flow, a 3-D displacement field is computed. (5) Finally, we estimate for each slice a linear or nonlinear transformation that we apply to the original 2-D slices to obtain a smooth volume.

We illustrate on Fig. 1 the steps of our method. To facilitate visualization, we use a 2-D toy example, in which a horizontal line is the analogue of a 2-D histological slice. Misalignment of histological slices within a stack is simulated by horizontally translating these lines, with values randomly drawn from a zero-mean normal distribution (Fig. 1 (a)). The aim of our technique is then to generate a smooth "reconstruction", visually similar to the unperturbed original source image, our ground truth here.

Approximating the 3-D volume

The first step of our method consists of obtaining a globally coherent 3-D volume from the input sequence of 2-D slices. Here we opted for a standard pair-wise reconstruction approach where consecutive pairs of 2-D slices are globally rigidly registered with the block-matching algorithm of Ourselin et al. (2000), owing to its robustness to artefacts and noise. Note that the smoothing approach presented in this manuscript is independent from the choice of a reconstruction technique for this first step. In particular, should some sections be affected by sever artefacts, the graph-theoretic based method of Yushkevich et al. (2006) could be used to skip the most distorted slices and prevent gross aberrations in the reconstructed volume.

In Ourselin et al.'s (2000) approach, displacement vectors are first computed by finding for each block in the source image a corresponding block in the target image, where correspondence is defined as the maximum of the chosen similarity measure, the correlation coefficient. The set of displacement vectors between all corresponding blocks forms a displacement field from which a rigid transformation is estimated in the least square sense. The influence of outliers caused by morphological differences between sections or background artefacts is mitigated by the use of a robust least-trimmed squares (LTS) regression (Ourselin et al., 2000).

Such pair-wise reconstruction strategy requires the choice of a reference section, which we pick as the middle slice in the stack.

As an illustration, Fig. 1(a) simulates a 2-D image reconstructed from individual 1-D lines. Image 1(a) may be seen as a cross-section view through a reconstructed 3-D volume.

Extracting the boundaries of interest

As argued in the Introduction section, the initial reconstruction is unlikely to yield a smooth volume in the absence of an external reference. Since volume smoothness is usually best appreciated at the boundaries between visually homogeneous regions (e.g., anatomical structures or sub-structures), we propose to use the latter as surrogate for the smoothness of the overall volume. Note that because of the tessellated nature of histological slices, structures of interest

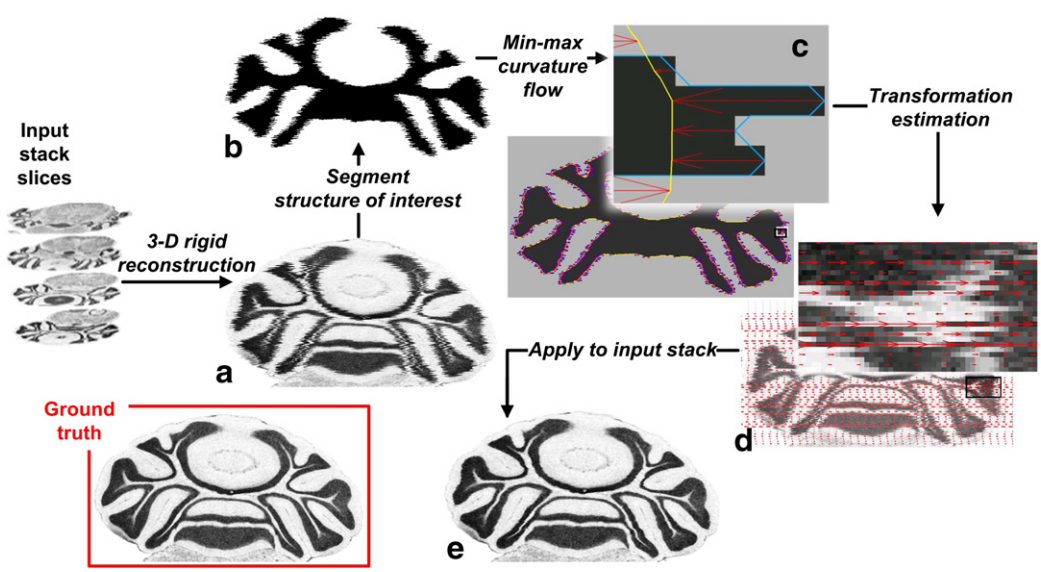

Fig. 1. The proposed smooth reconstruction applied to a 2-D toy example: (a) simulated cross-section cut (2-D image with randomly translated line, "Ground truth" corresponds to the unperturbed 2-D image); (b) segmented structure of interest: the gray–white matter boundary; (c) characteristic function (gray), front before (blue) and after (yellow) application of flow and computed sparse displacement field (red); (d) dense displacement field extrapolated from the global translations estimated on sparse field of (c); (e) result of smooth reconstruction obtained by applying the global transformations to input image (a). (For interpretation of the references to color in this figure legend, the reader is referred to the web version of this article.)

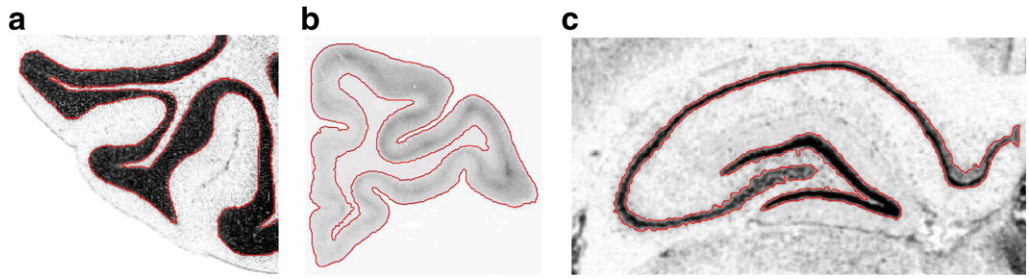

Fig. 2. Structures of interest (red) extracted from (a) a Nissl-stained histological slice of the mouse brain; (b) a immunohistochemistry processed slice of the monkey brain and (c) a Nissl-stained histological slice of the rat brain. (For interpretation of the references to color in this figure legend, the reader is referred to the web version of this article.)

can be found at a variety of scales. The selection of the appropriate boundaries should therefore depend on the overall goal of the application for which a histological volume is to be reconstructed. However, our curvature flow approach is flexible enough to allow for different structures to be used conjointly throughout a given stack of slices, or even the external contours of the organ or piece of tissue if no particular structure can be segmented. For instance, when reconstructing a whole rat brain from coronal sections, one could select the gray–white matter boundary in the cerebellum and in the hippocampus, and the outside contour for those sections anterior to the corpus callosum since they mostly consist of homogeneous gray matter.

This segmentation task is often complicated by the presence of intensity inhomogeneities. Those are usually due to variations in slice thickness, in the density of staining or in light condition during the digitization stage of the histological preparation process. Solutions from the literature usually consist in global intensity correction schemes based on histogram matching (Chakravarty et al., 2006; Dauguet et al., 2004; Malandain and Bardinet, 2003; Malandain et al., 2004). They normalize slice intensities by altering their overall distribution. Here, we selected the robust approach of Malandain and Bardinet (2003), which first computed a continuous probability density functions from the discrete intensity histograms of two input slices using a Parzen windowing technique and then estimated the optimal affine intensity transformation between them.

Next, the boundaries of the structures of interest are extracted. Depending on the characteristics of the input histological slices (contrast, signal to noise, etc.) more or less sophisticated segmentation approaches may be used. For the data presented in this paper, a simple intensity thresholding of the intensity corrected 2-D images followed by mathematical morphology was sufficient to segment the gray–white boundaries. Fig. 2 outlines in red the segmented structures of interest extracted from (a) a Nissl-stained histological slice from the cerebellum region of the C57BL/6 mouse brain,[1] (b) a immunohistochemistry processed slice of the frontal cortex of a *Macaca fascicularis* monkey brain[2] and (c) a Nissl-stained histological slice from the hippocampus region of a Wistar Hannover rat brain. Note that it is not crucial for this segmentation process to be completely accurate since we only use the extracted surfaces as surrogates. Our approach should accommodate situations where the structure's boundary is only approximately delineated as long as the smoothness of the extracted surface is representative of that of the initial volume reconstruction. Although we performed independent segmentations in 2-D for each slice, which did not require a 3-D volume to be reconstructed *a priori*, a 3-D segmentation approach could have been used alternatively.

In our toy example, the structure of interest, the gray-white matter boundary (Fig. 1(b)), is outlined in blue in Fig. 1(c).

3-D Min–max curvature flow constrained to 2-D plane

To improve upon the lack of smoothness of the 3-D volume generated in step (1), we propose to smooth the extracted surfaces with a min–max curvature flow (Malladi and Sethian, 1996). This data-driven curvature flow consists in evolving the input surfaces (or "front") along their normal direction, with speed dependent on their curvature and local topology.

Mathematically, this motion (or flow) is described by a system of partial differential equations (PDE). An attractive solution for the PDE system was proposed by Osher and Sethian (1988). They model the evolving front, Γ, as the zero level set of a higher dimensional function, ϕ. Such an implicit representation of the front presents a number of advantages over an explicit one (Osher and Fedkiw, 2002): the geometrical position of any point with respect to the front is easily identified, the normal direction and curvature may be computed at any point etc. In particular, topological changes (merges and breaks) occurring during the evolution of the front are easily dealt with.

The min–max flow is built around a switch function which controls whether the front should move inward, outward or not at all. Following Ref. (Malladi and Sethian, 1996), we use the following switch function:

$$F_{min/max} = \begin{cases} min(\kappa, 0) & avg^{r}_{\phi(x,y)} < 0, \\ max(\kappa, 0) & \text{otherwise} \end{cases} \tag{1}$$

where $avg^{r}_{\phi(x,\,y)}$ is the average of intensities of ϕ in a neighborhood of radius r centered at (x, y). r determines the scale at which smoothing will occur. We took ϕ as the "signed" characteristic function computed from the segmented surface:

$$\phi(x,y) = \begin{cases} -1 & (x,y) \in \Omega, \\ +1 & \text{otherwise} \end{cases} \tag{2}$$

where Ω denotes the inside of the extracted surface. Note that the min–max flow has been extensively used as image smoothing and noise filtering technique (Malladi and Sethian, 1996; Malladi and Sethian, 1997), with the iso-contours of the image as level set function.

For the purpose of our histological reconstruction application, this isotropic min–max flow is not entirely suitable, since the cutting axis plays a different role from the other two orthogonal directions (Malandain et al., 2004). Indeed, movement along the direction of the sectioning plane (across slices) is undesirable since we need to extract from the flow independent slice transformations. Therefore, we confine the min–max flow to the planes in which the slices reside, by restricting the motion along the cutting axis (the third component

[1] http://map.loni.ucla.edu.
[2] http://www.brainmaps.org.

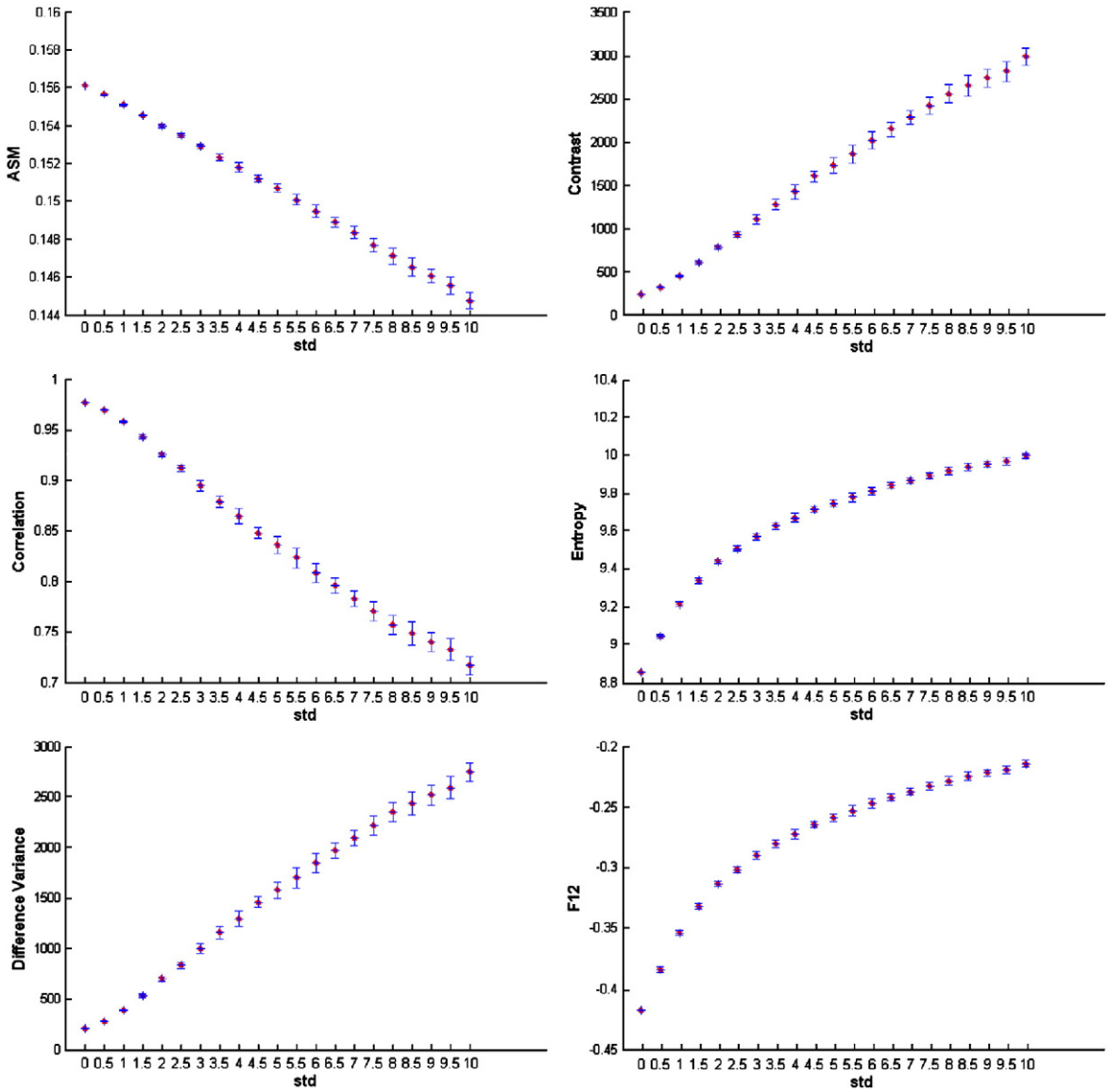

Fig. 3. Mean (red) and standard deviation (blue) of features computed for a perturbed 2-D data set. (For interpretation of the references to color in this figure legend, the reader is referred to the web version of this article.)

of the 3-D space here). Taking into account this constraint and plugging the min–max speed function into the general level set equation (Osher and Sethian, 1988):

$$\phi_t + F\nabla\phi = 0 \tag{3}$$

we derive the following flow equation:

$$\phi_t = \left[\left(F_{min/max}, F_{min/max}, 0\right)\cdot\left(\frac{\nabla\phi}{|\nabla\phi|}\right)\right]\cdot\nabla\phi \tag{4}$$

Note that this constraint mitigates shrinkage of the volume along the cutting axis while still allowing for the curvature and normal direction to be computed in 3-D.[3]

The condition $\mathrm{avg}^{r}_{\phi(x,\ y)}<0$ is evaluated once for a given value of r and the surfaces are evolved until the flow stops. We previously presented a similar smoothness approach in Ref. (Cifor et al., 2009), where a constrained mean curvature flow was used, instead, to smooth the extracted boundaries. Whereas in a classical mean curvature flow the front evolves towards completely convex shapes and shrinks before ultimately disappearing, min–max curvature flow smooths out only those features of the front that are smaller than a given scale. This scale-dependency makes it particularly amenable to our problem. Indeed it then becomes possible to tackle the "jagged" aspect of the extracted surfaces while preserving their global shape. Furthermore, the flow may be applied either independently to each surface, or once to all extracted boundaries of interest. Finally, min–max flow stops once features smaller than the selected scale have been smoothed, at which point the front stays constant. This removes the need for an external termination criterion.

Estimating individual slice transformations

The last step of our method consists in estimating the independent transformations corresponding to each individual slice. The motion of the front throughout the entire flow may be tracked within each slice from the discretization of the equation of motion. The trajectories of each point on the front can then be summarized in a displacement field, from which a transformation corresponding to each slice is

[3] The described scheme was implemented on top of the LS Toolbox for matlab http://www.cs.ubc.ca/mitchell/ToolboxLS/.

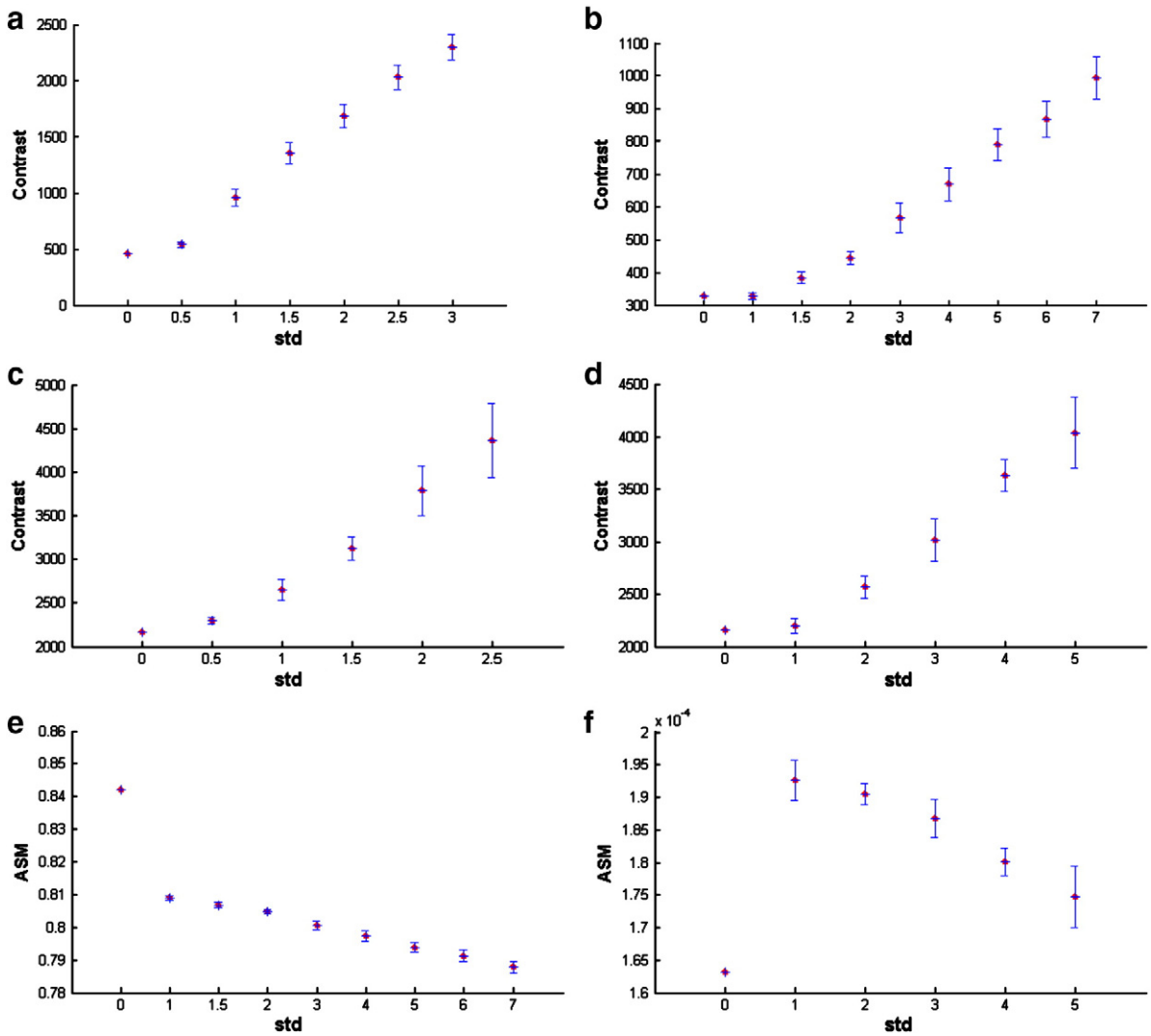

Fig. 4. Mean (red) and standard deviation (blue) of contrast computed for a 3-D MRI perturbed by random translations (a) and rotations (b); a 3-D histological volume perturbed by random translations (c) and rotations (d). Mean (red) and standard deviation (blue) of ASM computed for a 3-D MRI perturbed by random rotations (e) and 3-D histological volume perturbed by random rotations (f). (For interpretation of the references to color in this figure legend, the reader is referred to the web version of this article.)

estimated. A straightforward way to find the change in position of each front-point, x on the front, after time-step Δt, would be to directly compute the displacement from the discrete form of the equation of motion, along the normal direction. However, composing displacement vectors between the initial and final position of the front, based on the values of the level set function alone is unlikely to be accurate due to the numerical errors induced by the discretization of the equation of motion.

Moreover, the level set function chosen here is a characteristic function, which does not inform us of the distance between points situated away from the front. Note that even if we used a signed distance map (an euclidean distance approximation) as implicit representation of the front (i.e., as level set function), the overall displacement field would still lack accuracy because such function does not remain a distance map throughout the entire run of the flow.

A remedy to this problem is proposed by Ref. (Gomes and Faugeras, 2000). It consists in modifying the original PDE by taking into account the fact that all the points along a characteristics of the level set function have the same curvature. Indeed the characteristics of a distance map are in fact straight lines. Therefore, they suggest to track the position of the front at each iteration, following the characteristic rays. Inspired by this idea, we search iteratively for the new position of the front in the direction of motion. We look for the zero-crossings of the level set function, after each flow iteration, starting at the last known position of the front. The overall displacement vector is then obtained by composing these small intermediary vectors.

Fig. 1(c) shows in yellow the front after its evolution under our constrained min–max curvature flow formulation, for $r=\{1,2\ldots,6\}$, and the computed sparse displacement field in red. Note that the displacement field is indeed purely horizontal as the flow is restricted to the horizontal direction.

Since we extract an actual displacement field from the flow, we can offer a large choice of transformation spaces to be applied to the individual slices, from global rigid or affine to arbitrarily flexible ones. Maximal flexibility is obtained by extrapolating the sparse displacement fields to the whole slices, and applying the resultant fields directly to the original histological sections. This mimics the motion described by the flow and is independent for each slice. For intermediate results, the adaptable rigidity approach of Ref. (Pitiot and Guimond, 2008) could be used to regularize the field corresponding to individual slices. In this approach, the regularization is informed by the 2-D topology and geometry of the slice and its flexibility is controlled by the size of a rigidity radius. Small values of the radius capture local distortions, while larger values give more rigid transformations. Finally, we can estimate global rigid and affine

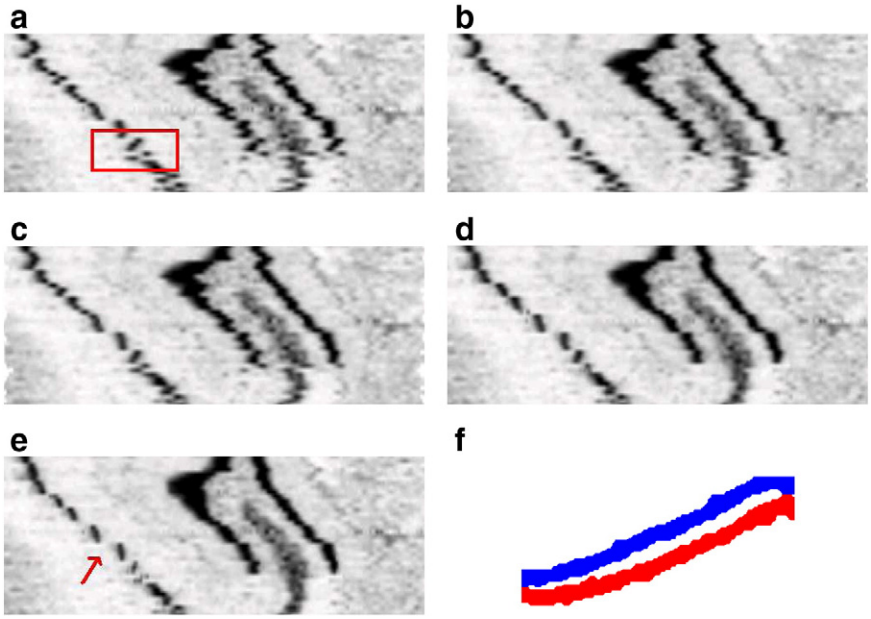

Fig. 5. Sagittal view in hippocampal region of a Wistar Hannover rat brain reconstructed using: (a) pair-wise globally rigid block-matching; (b) global rigid transformations estimated from min–max flow; (c) global affine transformations estimated from min–max flow; (d) after rigidity adaptable regularization of the displacement field extracted from min–max flow; (e) direct application of the displacement field extracted from min–max flow; (f) coronal view of the gray matter bands segmented in the region highlighted in red in (a) in two adjacent slices (one in blue and one in red). (For interpretation of the references to color in this figure legend, the reader is referred to the web version of this article.)

transformations for each slice, with a robust least square regression algorithm (the LTS of Ref. (Rousseeuw, 1984) for instance).

Quantifying smoothness

As mentioned earlier, smoothness is typically evaluated by visual inspection of the 3-D reconstruction. A quantitative assessment of smoothness is challenging in the absence of information about the original shape of the 3-D structures. The available literature on the subject mostly focuses on measuring the distance between pairs of corresponding points across adjacent sections, based on the hypothesis that the small thickness and intrinsic characteristics of histological slices ensure that such distances should be minimal (Guest and Baldock, 1995; Ju et al., 2006). A departure from those, Baheerathan et al. (1998) proposed an intensity-based technique relying on three textural descriptors (angular second moment (ASM), contrast and correlation) (Haralick et al., 1973), computed from gray-level co-occurrence matrices, GLCMs, to assess the 3-D reconstruction of cellular structures from TEM sections of mouse liver cell nuclei.

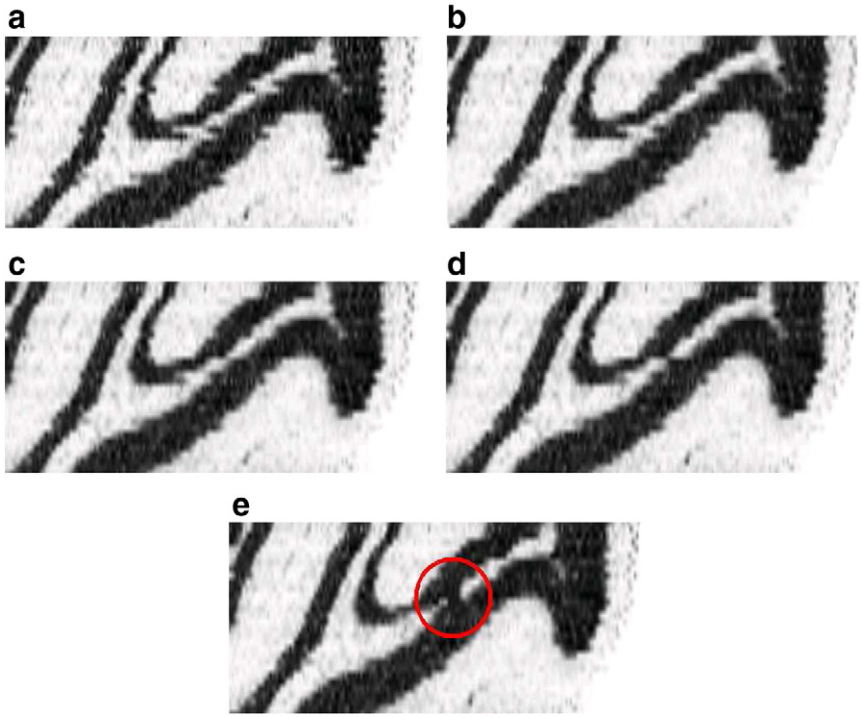

Fig. 6. Sagittal view of the LONI C57BL/6 mouse brain reconstructed using (a) pair-wise globally rigid block-matching; (b) global affine transformations estimated from min–max flow; (c) and (d) same with rigidity adaptable regularization of the displacement field extracted from min–max flow; (e) after the direct application of the displacement field.

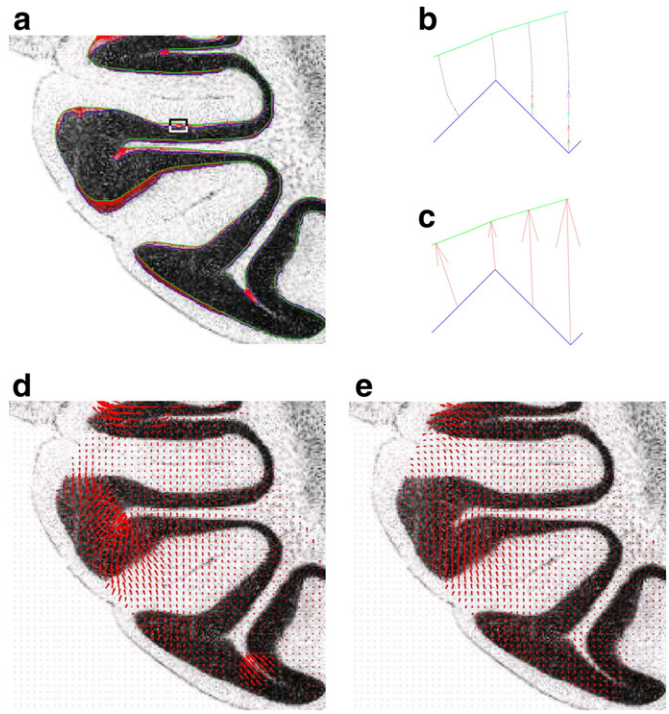

Fig. 7. (a) Coronal slice from the LONI C57BL/6 mouse brain with the front before (blue) and after (green) mix–max curvature flow and sparse displacement field (red); (b) step-by-step computation of the magnified field in (c); (d) extrapolated dense displacement field; (e) displacement field regularized with the rigidity adaptable approach. (For interpretation of the references to color in this figure legend, the reader is referred to the web version of this article.)

In this article we too choose to quantify smoothness based on intensity rather than points, which frees us from the pitfalls associated with point extraction (limited coverage, position biases, etc.). Rather than limiting ourselves to the case where the structures of interest are circular or oval, with overall orientation of the 3-D cellular structure perpendicular to the cutting axis as in Ref. (Baheerathan et al., 1998), here we consider more complex structures with arbitrarily 3-D shape and orientation.

Selecting the best descriptor

We selected a number of GLCM-based textural features and evaluated their ability to quantify the smoothness of reconstructed volumes. Appendix A gives the formal definition of GLCMs and the textural features used here. Those are representative of the textural classification given by Ref. (Gotlieb and Kreyszig, 1990): (1) ASM, contrast and correlation define visual textual aspects; (2) difference variance is a statistics-based classifier; (3) entropy; and (4) information measure of correlation f_{12}.

GLCMs encapsulate 2nd order moments and summarize the frequency with which pairs of intensity values occur in an image at a given distance and angular direction. Since we are interested in the smoothness of the volume *along* the cutting axis, we chose distance = 1 and picked as a direction the one going across slices. We also chose not to quantize intensities in spite of the associated computational penalty since grouping the intensity values into larger bins will inevitably contribute to a loss of textural information. In particular, small-scaled details along the boundaries of interest may be lost.

In order to analyze the behavior of the selected textural features, we perturbed three different datasets with random rigid transformations extracted from a zero mean normal distribution of increasing standard deviation (std). Fig. 3 plots the mean (red) and standard deviation (blue) of the features for the first dataset: the 1-D example of Fig. 1(a). For each value of *std*, we generated 30 images and the horizontal translations are applied using nearest neighbor interpolation.

In a similar fashion, we perturbed the (x, y) planes of a T1-weighted 0.65 mm isotropic MR scan of the visual cortex of the human brain, dataset 2, with random translations and rotations (20 volumes per std) with bilinear interpolation. The mean and standard deviation of the contrast values are displayed in Fig. 4(a–b) and the ASM values for the volumes obtained by random rotations are shown in (e).

Finally, dataset 3 consists in a histological volume of the C57BL/6 mouse brain[4] reconstructed with our smoothness-guided technique (Cifor et al., 2009) and perturbed by random translations using nearest neighbor interpolation and rotations using bilinear interpolation. We generated 10 volumes per std after padding the original volume with a border large enough to accommodate those perturbations in order to avoid loss of information at the image borders (the padding values were chosen outside the normal intensity domain not to interfere with the computation of the GLCMs). Before we compute the features, the entries corresponding to pairs of voxels involving border ones are set to zero such that only pairs of intensities within the area of overlap between neighboring slices will be considered. Fig. 4(c–d) show the contrast values computed for these volumes and Fig. 4(f) the ASM values for the histological volume perturbed by random rotations only.

We note that the textural features increase or decrease together with the smoothness of the structures of interest. While they all behave well when nearest neighbor interpolation is used for resampling (see Fig. 3), the ASM, entropy and f_{12} descriptors are more sensitive to bilinear interpolation than contrast, correlation and difference variance. Notice in particular the difference between contrast and ASM in Fig. 4(b) and (e). In the case of histological volumes perturbed by random rotations (dataset 3), ASM, entropy and f_{12} do not match the human perception of decreasing smoothness unlike contrast, correlation and difference variance. In this case we considered the intensity values in the area of overlap across slices (i.e., the padded border was avoided in the computation of the GLCM).

Contrast as smoothness quantifier

Our experiments indicate that the contrast, correlation and difference variance descriptors could equally be used as smoothness measures. Following the analysis of Gotlieb and Kreyszig (1990) which singled out contrast has the most discriminant descriptor for classification, we pick it as our measure.

The contrast descriptor measures the amount of local variation in a textured image. A closer look to its definition (A.6) confirms that the larger the difference between the two intensity values of a given voxels pair, the higher the contrast value. A jagged and distinguishable boundary will then produce numerous pairs of significantly contrasted intensity values, along the cutting axis. Therefore, it is reasonable to assume that along a smooth boundary, much fewer such pairs will be found and the value of the contrast descriptor will be smaller.

In practice, it is desirable to compute the GLCMs that capture the characteristics of the reconstructed volumes in the neighborhood around the extracted surfaces, rather than compute them over the whole volume. In addition to improving computation speed, this also prevents artefacts and noise away from the surface to impact the measure of smoothness of the surface. The narrow band can be defined by a neighborhood around the zero-level set of the signed distance map computed for the segmented boundaries of interest. Consequently, we adjust the size of the narrow band with a threshold over the signed distance map and consider only those voxels with corresponding signed distance map values in the given range. By discarding pairs of intensities in the computation of the GLCM, the memory consumption is also greatly reduced.

[4] http://www.loni.ucla.edu.

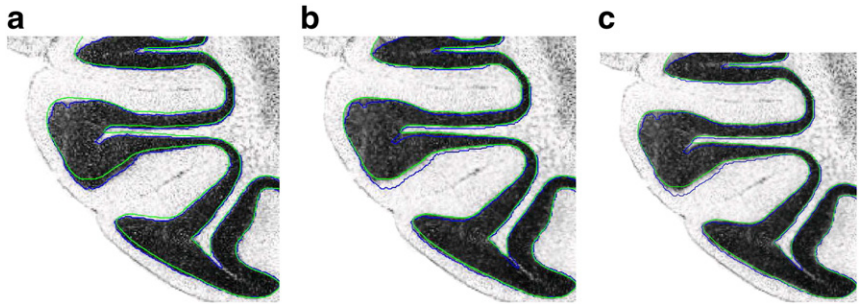

Fig. 8. (a) Original slice after pair-wise reconstruction and after (b) min–max displacement field is applied to it and (c) with rigidity adaptable approach.

Results

We present a selection of reconstruction results obtained from both synthetic and real datasets. In addition to showing figures, we also report values from our smoothness measure. We also investigate the robustness of our approach to a variety of noise, segmentation and alignment issues.

Hippocampal region of the rat brain

We applied our smooth reconstruction approach to a set of 210 Nissl-stained histological sections, cut coronally from a Wistar Hannover rat brain. The scale used in the min–max flow was $r=1$. Fig. 5(a) shows a typical pair-wise rigid reconstruction result (step 1 of our method) in the region of the hippocampus. The reconstructed volumes obtained by estimating rigid and affine transformations from the min–max flow are displayed in (b) and (c). Note that even though both volumes in (a) and (b) are obtained by applying global rigid transformations to the input slices, our technique managed to produce a more visually pleasing reconstruction. A more flexible transformation space was used in (d), where we employed the rigidity adaptable regularization (Pitiot and Guimond, 2008) of the displacement field, with a radius = 10. Finally, a direct application of the min–max field to the individual slices of the volume in (a) yielded an even smoother volume in (e). Note that each of the volumes in panels (b–e) is obtained from the volume in (a).

We also computed the contrast feature from GLCMs taken in a narrow band around the extracted surfaces. For the volumes shown in Fig. 5 we get the following contrast values: contrast $(a)=4665.6$, contrast $(b)=3314.4$, contrast $(c)=3094.2$, contrast $(d)=2339.6$ and contrast $(e)=2124.3$, which confirms that the more visibly smooth the volume, the lower the contrast.

As mentioned above, by rigidly registering the stack of slices as a first step, we build a 3-D coherent approximation of the anatomical structures. However, when there is little or no overlap between structures segmented on neighboring slices, steep curvature values may induce discontinuous smoothed 3-D volumes. As an illustration, Fig. 5(f) shows the superposition of the gray matter bands segmented within the region highlighted in red in Fig. 5(a) on two consecutive slices. The fact that they do not overlap induced a discontinuity in the reconstructed volume (red arrow in Fig. 5(e)).

Cerebellum region of the mouse brain

Fig. 6 shows a sagittal view of the histological volume reconstructed from a set of 350 50 μm Nissl-stained coronal sections of the C57BL/6 mouse brain from the LONI database.[5] The initial pair-wise rigid reconstruction is displayed in (a). A smoother reconstruction obtained with global affine transformations estimated from the min–max flow for each slice is presented in (b). The volumes in (c) and (d) are obtained by applying the displacement field after regularization with the rigidity adaptable approach (Pitiot and Guimond, 2008), using radii of 25 and 15, respectively. The volume obtained by directly applying the displacement field computed from the flow is displayed in (e).

Note that, even though direct application of the displacement field yielded the smoothest volume, it also induced a collapse of the cortical ribbon in the region highlighted in red. This reflects the fact that min–max curvature flow merged the two fronts at this location. This effect is largely alleviated when a local regularization is used (c and d).

The corresponding contrast values are contrast $(a)=3635.7$, contrast $(b)=2580.3$, contrast $(c)=2323.8$, contrast $(d)=2239.5$ and contrast $(e)=2099.4$. Without surprise, using a smaller radius for the regularization of the displacement field in (d) leads to more flexible transformations to be estimated from the flow and, therefore, to a smoother volume than in (c). Maximum flexibility is obtained in (e).

Fig. 7(a) shows the overall displacement field computed from our min–max flow in one particular histological slice in the stack. A magnified view of the field between the initial (blue) and final (green) position of the front is shown in (c) with its step-by-step evolution in (b). In (d), we present the extrapolated field using bilinear interpolation and, in (e), the regularized field with the rigidity adaptable approach. The corresponding slices transformed by applying those two fields are shown in Fig. 8(b) and (c). For visual comparison, we present the original slice with its segmented boundary in blue and final position of the front in (a). We note indeed that the regularized field preserves the shape of the gray matter ribbon at high curvature regions in (c), as opposed to (b) where the flow tends to smooth them.

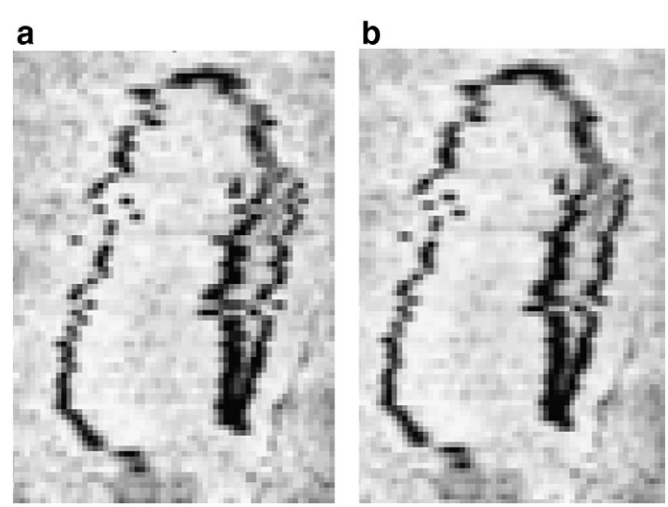

Fig. 9. (a) Initial pair-wise rigid reconstruction; (b) after rigid transformations estimated from min–max displacement field are applied to it.

[5] http://map.loni.ucla.edu.

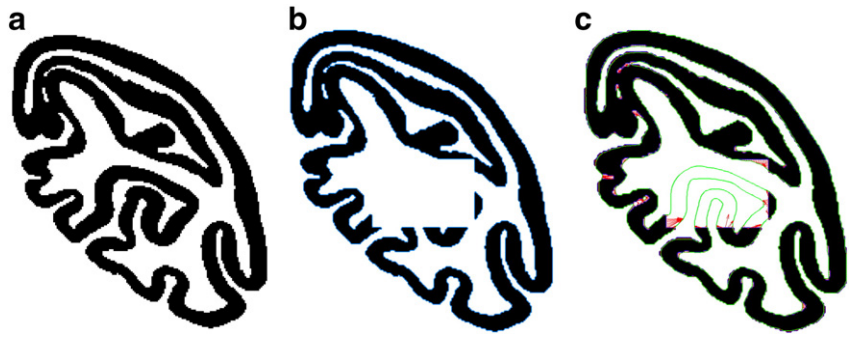

Fig. 10. The influence of a hole: (a) boundaries of interest extracted from coronal slice in monkey brain sample; (b) same slice and associated front (blue) after a rectangular region was removed; (c) the front before (blue) and after (green) min–max curvature flow was applied with displacement field in red. (For interpretation of the references to color in this figure legend, the reader is referred to the web version of this article.)

Entire mouse brain reconstruction

Fig. 16 displays transversal (left) and sagittal (right) views of the entire C57BL/6 mouse brain reconstructed with our min–max approach in order of increasing flexibility of the transformation estimated from the flow (from least flexible at the top to most flexible at the bottom). We selected as boundaries of interest the gray–white border within the hippocampal and cerebellum regions as we observed clear jaggedness there. As an illustration of the ability of our technique to offer fine control over the reconstruction process, we applied the flow independently to each structure with different values for radius r: $r=\{1,2\}$ in the cerebellum area and $r=1$ in the hippocampal region.

Fig. 16(b) shows that although we did not improve smoothness over the initial pair-wise reconstruction in the cerebellum region when estimating rigid transformations, we did make a visible improvement in the hippocampal region (see also Fig. 9 for an enlarged side-by-side comparison). A smoother reconstruction is obtained in both regions when global affine transformations were estimated for each slice (Fig. 16(c)).

As in the previous examples, the rigidity adaptable approach does not suffer from the artefacts caused by over-smoothness when the estimated displacement field is directly applied to the slices (see in particular the cerebellum region).

The contrast values for the reconstructions in Fig. 16 are contrast $(a)=1937.5$, contrast $(b)=1584.6$, contrast $(c)=1415$, contrast $(d)=1358.1$ and contrast $(e)=1237.3$. Note that these values are obtained from the intensity values within neighborhoods of the segmented structures of interest.

Robustness to segmentation issues

We conducted a number of experiments to assess the performance of our method when the boundaries of interest were less accurately segmented.

We first simulated the effect of a hole or tear by removing a rectangular region in one Nissl-stained coronal slice from the cortex region of a monkey brain stack (*Chlorocebus aethiops*)[6] (Fig. 10(b)). We then applied our min–max curvature flow to the gray–white matter and pial boundaries with $r=1$. Fig. 10(c) shows this particular section's front before and after the flow, together with the extracted displacement field. Note how the flow managed to extrapolate the missing parts of the gray–white matter boundary (green contour) based on information from adjacent slices. Unsurprisingly, the displacement field computed in this region is meaningless since our approach only tracks points along the initial front which was incomplete because of the hole. The missing information could potentially be recovered using the content of the neighboring slices, e.g., by cross-slices interpolation.

Fig. 11 illustrate the behavior of our reconstruction approach when holes or tears extend over several slices. We used rectangular parallelepipeds of thickness 5 slices on average and ran the flow with radii up to 2 and 3. The volumes obtained by applying the displacement field directly to the slices are displayed in (b) for $r=\{1,2\}$)and (c) for $r=\{1,2,3\}$. Here, the boundaries of the structure not affected by the holes have been smoothed adequately and the influence of the holes has been alleviated in places, where the flow helped interpolate missing information. Global affine transformations estimated from the flow also produce smoother volumes in (d) and (e) than the initial rigid reconstruction in (a). Those volumes are similar to the ones obtained with global affine transformations estimated from corresponding flows without patches and shown in (f) and (g). Slightly less smooth boundaries than in (f) are visible in the right-hand side corner of volume (d), due to missing information. However, overall the flow copes well with the missing information and the resemblance between the pairs of volumes (d, f) and (e, g) is an indicator of its robustness.

Next, we measured the influence of locally perturbed extracted boundaries, as would be obtained from noisy input slices. We illustrate in Fig. 12 the effect of applying a varying amount of salt and pepper noise to an accurate segmentation of the gray–white matter and pial surfaces of the monkey brain sample (left column). The top and bottom rows show what happened to the front after we applied our min–max flow to a segmentation mask in which we randomly switched 50% and 70% of the pixels, respectively. We show the front after min–max flow with $r=1$ (middle column) and after an additional smoothing step with $r=2$ (right-most column).

In addition to severely perturbing the initial boundaries, salt and pepper noise creates superfluous contours. When those are smaller than the chosen r (for $r=1$, at 50% noise, and for $r=2$ at 70% noise), they are easily discarded by min–max flow, as was initially noted by (Malladi and Sethian, 1996).

In the last part of our analysis, we chose two structures of interest on the coronal slices of the monkey brain: the gray matter ribbon (Fig. 13(b)) and the outline of the tissue extracted from the slice (Fig. 13(c)). Note that the segmentation (c) does not give much information about the geometry (shape, location etc.) of the structures *within* slices. We apply the flow using the two types of segmentation and present in Fig. 14(a–b) the volumes smoothed with global affine transformations estimated from each displacement field. We note that the reconstructions give very visually similar smoothed volumes, with corresponding contrast values: contrast $(a)=1190.8$ and contrast $(b)=1139.3$. While this does not constitute a proper validation, it illustrates an effect that we repeatedly observed throughout our experiments.

We also compared those reconstructed volumes to the one obtained with a classic pair-wise affine reconstruction of the

[6] http://www.brainmaps.org.

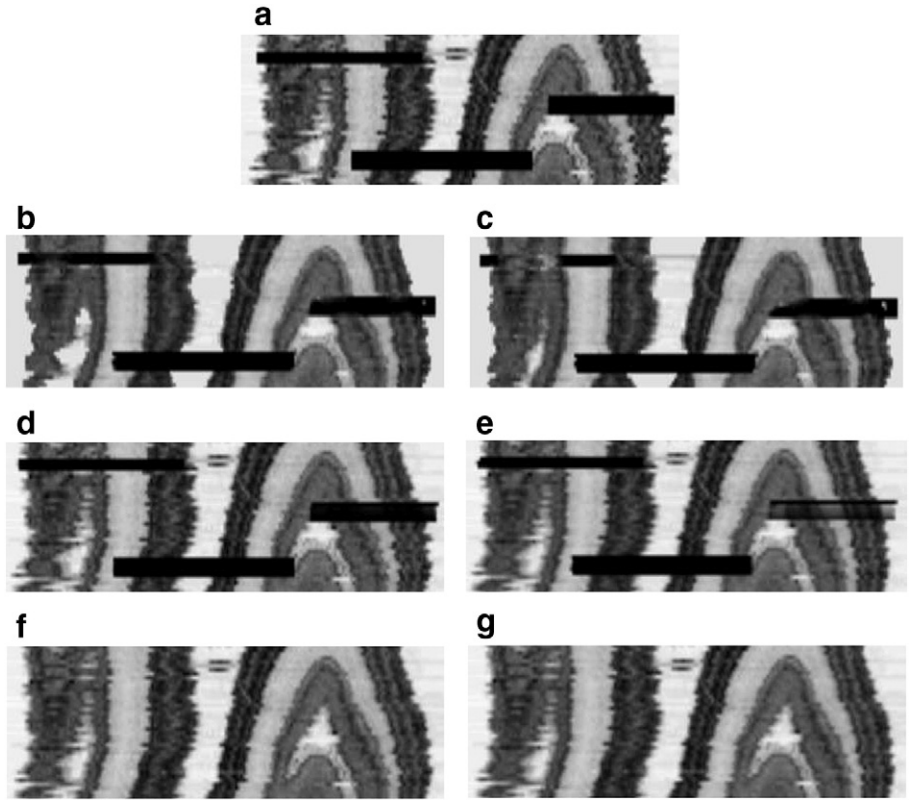

Fig. 11. The influence of overlapping holes: (a) original pair-wise rigid reconstruction with holes; (b) volume (a) smoothed by direct application of the displacement field computed from the flow with $r=\{1,2\}$; (c) same with $r=\{1,2,3\}$; (d) global affine transformations estimated from flow with $r=\{1,2\}$; (e) same with $r=\{1,2,3\}$; (f) global affine transformations estimated from flow with $r=\{1,2\}$ applied to original reconstruction; (g) same with $r=\{1,2,3\}$.

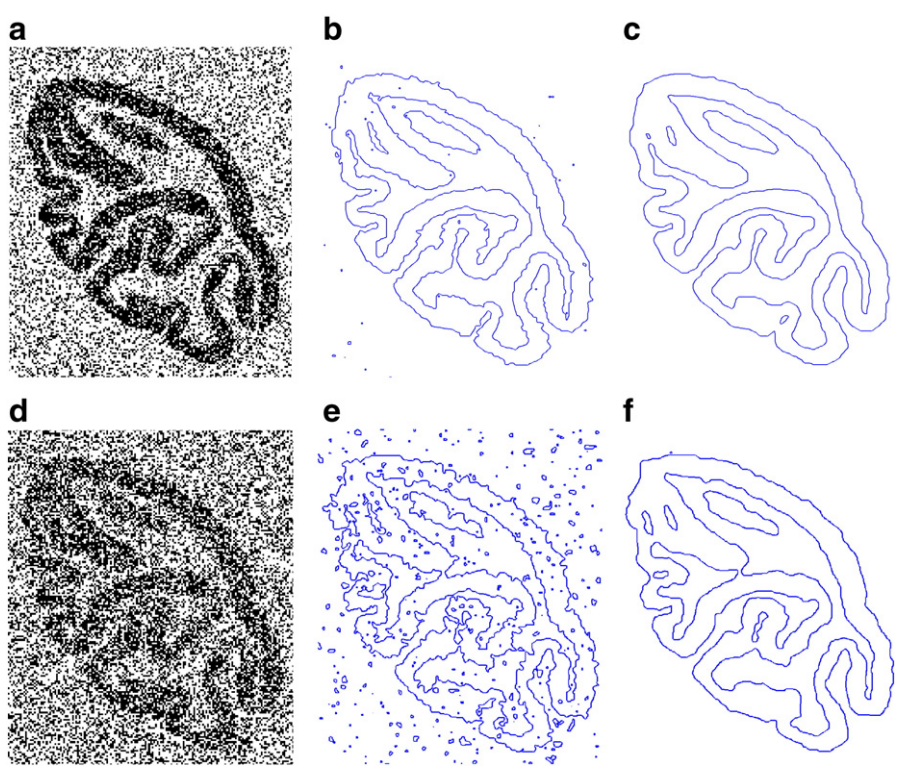

Fig. 12. A slice from segmented volume perturbed with (a) 50% and (d) 70% salt-and-pepper noise; (b) and (e) show the corresponding fronts smoothed with constrained min–max curvature when $r=1$; (c) and (f) are the fronts after the flow continued for $r=2$.

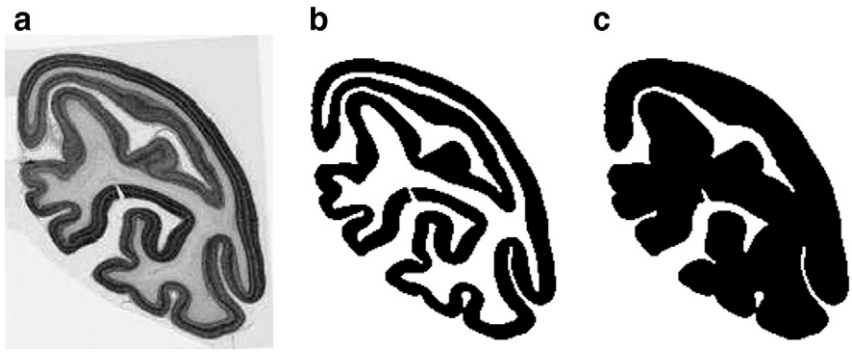

Fig. 13. Nissl-stained histological slice of monkey brain: (a) original slice; (b) and (c) segmented structures of interest.

Fig. 14. Sagittal view of the volumes obtained by global affine transformations estimated from the flow applied to: (a) the gray–matter boundaries and (b) the outline of the whole structure of interest. (c) Sagittal view of the volume obtained by pair-wise affine registration. (For interpretation of the references to color in this figure legend, the reader is referred to the web version of this article.)

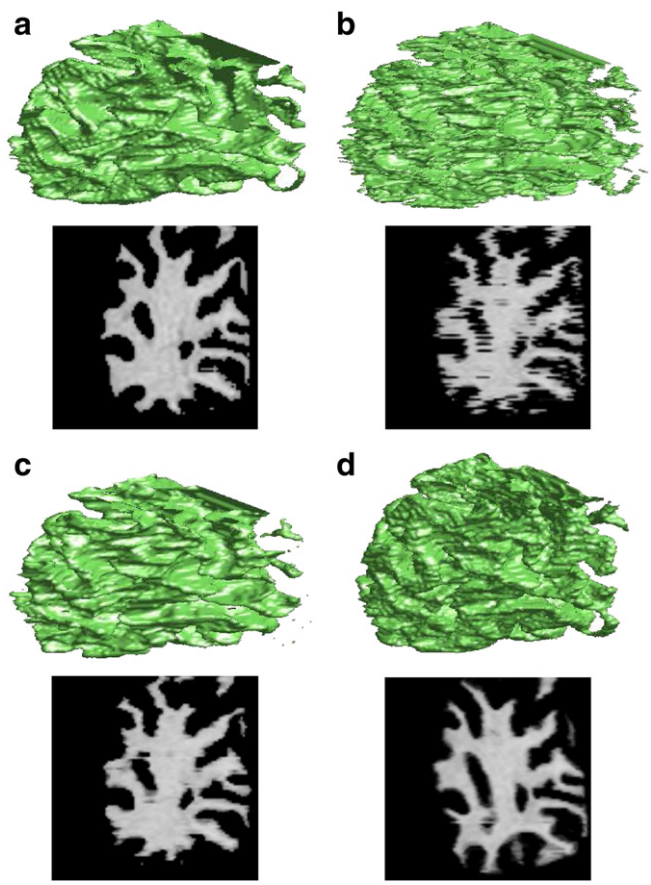

Fig. 15. Smooth reconstruction of artificially perturbed MR volume: (a) gray–white matter surface segmented from MRI (top) and the cross-section view (bottom); (b) surface extracted from set of perturbed sections (top) and its cross-section view (bottom); (c) same after min–max curvature flow; (d) same after pair-wise rigid reconstruction. (For interpretation of the references to color in this figure legend, the reader is referred to the web version of this article.)

unregistered stack of slices (Fig. 14(c)). While the latter is also both visually and quantitatively smooth (contrast $(c) = 1105.6$), it presents a more tubular shape due to the aperture problem and the accumulation and propagation of errors led to distortions visible in the region pointed by the red arrow.

Robustness to initial pair-wise alignment

In order to circumvent the lack of ground truth associated with histological volume reconstruction, we propose to assess the robustness of our method to the initial pair-wise alignment on the high resolution 0.65 mm isotropic in-vivo T1-weighted MR scan of the human brain, which we can artificially perturb (Fig. 15). As with our toy example, we simulate a rough global rigid reconstruction by applying to the individual slices of the MR volume random rigid transformations drawn from a zero-mean normal distribution of gradually increasing standard deviation. We then apply our reconstruction technique to the set of perturbed slices. The quality of the reconstruction can then be estimated by measuring its deviation from the original, unperturbed, MR volume.

Numerical results are given in Table 1. σ_t and σ_r denote the standard deviation of the random translations and rotations applied to the slices of the original MR volume, O. For each value of σ_t andσ_r, we generated 5 perturbed volumes. We report the mean and standard deviation of the Dice coefficient (a measure of volume overlap (Dice, 1945)) computed between the original MR and: the perturbed volumes, T; the volumes obtained by directly applying the displacement fields extracted, for each slice, from the min–max curvature flow, M; and the volumes obtained by applying rigid transformations estimated from the displacement fields, R. In order to show the influence of the size of the neighborhood, r, on smoothness, we also computed the Dice coefficient for the volumes R reconstructed with rigid transformations extracted from the displacement field given by the flow with $r = 2$. Finally, we estimated a root–mean–square (RMS) error in each case as follows:

$$\mathrm{RMS} = \sqrt{\frac{1}{4N}\sum_{s=1}^{N}\sum_{i=1}^{4}\left(\|P_s^i - P^i\|^2\right)} \tag{5}$$

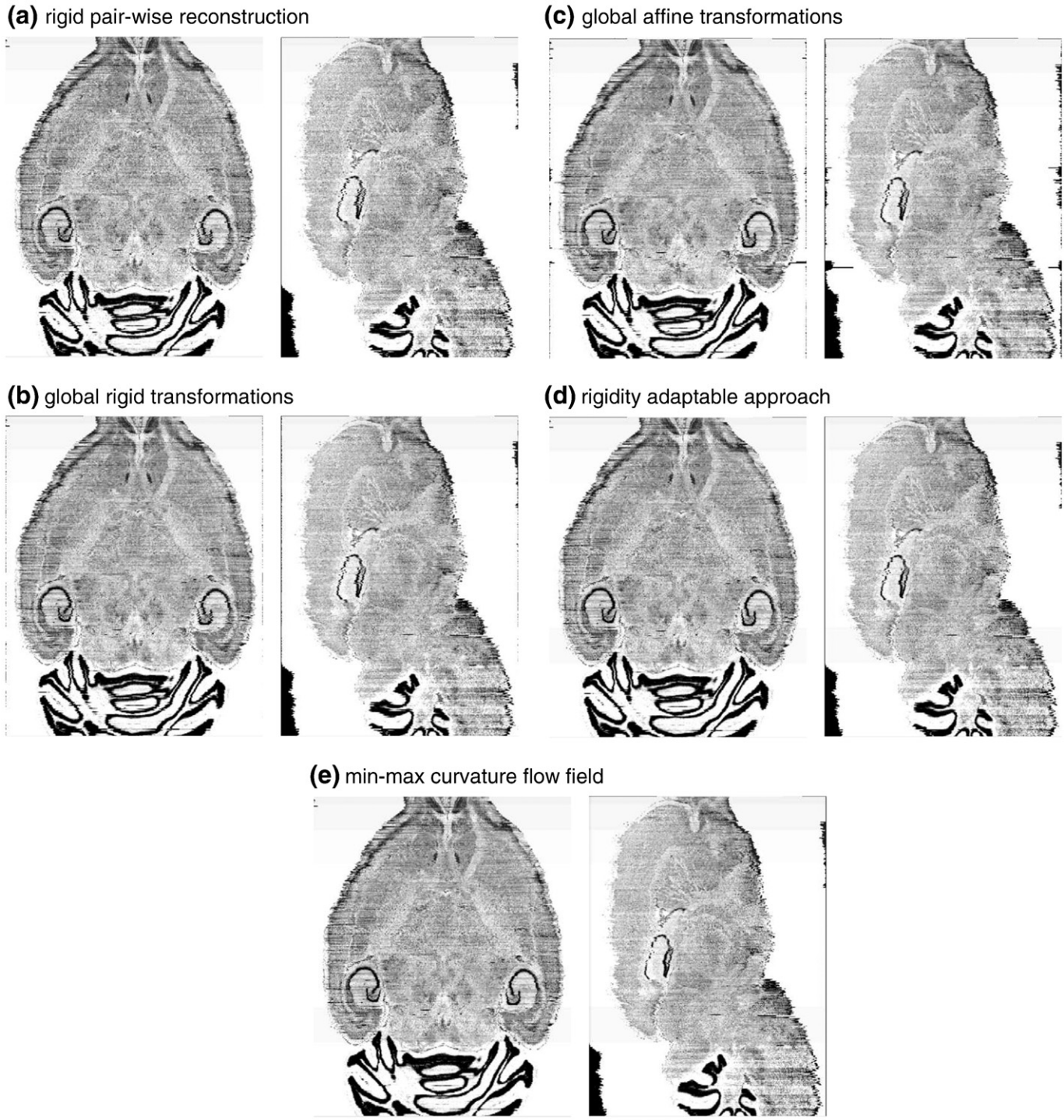

Fig. 16. Transversal (left) and sagittal (right) views of the C57BL/6 mouse brain reconstructed with increasing flexibility of the transformations estimated from the flow.

where N is the number of slices in the reconstructed volume, P_s^i are the coordinate of the four corners of slice s and P^i is the average coordinate across all slices for corner i. Such formulation gives RMS = 0 when the corners fall in perfect alignment across all slices, as is the case in the original, unperturbed, MRI.

Fig. 15(a) (top) displays the gray–white matter surface extracted from the original MRI. We show in (b) the surface obtained after application of random translations ($\sigma_t = 1$). Finally, we show in (c) the smoothed surface obtained with our min–max curvature flow, a close approximation of the original MR. For a visual comparison, we display in (d) the surface extracted from a rigid pair-wise reconstruction of those MRI slices.

Table 1 also includes the contrast values computed for the MRI volumes used to analyze our smooth-reconstruction technique in the previous section. Note that because the MR volume is tessellated, with structures present at a variety of scales, the flow will inevitably smooth out those smaller than the chosen radius r which may yield a reconstructed volume smoother than the original one (Fig. 15(c)).

Table 1
Validation results: see text for details.

Measure		$\sigma_t=1$	$\sigma_t=2$	$\sigma_t=3$	$\sigma_r=2$	$\sigma_r=3$	$\sigma_r=4$
Dice (%) (r = 1)	T	86.7 ± 0.4	77.9 ± 1	72.4 ± 0.8	89.1 ± 0.2	87.2 ± 0.5	85.1 ± 0.6
	M	89.6 ± 0.3	83.1 ± 0.7	78.3 ± 0.8	90.8 ± 0.1	89.5 ± 0.4	88 ± 0.6
	R	88 ± 0.2	80.5 ± 0.8	74 ± 0.7	89.4 ± 0.2	87.7 ± 0.5	85.7 ± 0.6
Dice (%) ($r=2$)	R	88.6 ± 0.1	82 ± 0.7	76.4 ± 0.7	89.6 ± 0.1	88 ± 0.4	86.1 ± 0.7
Contrast ($r=1$)	T	1822	3311	3496	947.3	1177.6	1409.2
	R	1162	2056.3	2550	713.9	873.7	1054.2
	M	886.6	1250.3	1332.3	581.6	628.6	687
	O	944.1	853.4	740.3	695.4	695.4	695.4
RMS (rigid)		0.87 ± 0.02	1.97 ± 0.1	3.1 ± 0.1	1.8 ± 0.1	2.7 ± 0.3	3.9 ± 0.4

This explains why the contrast value for M in Table 1, corresponding to $\sigma_t=1$ and σ_r, is less than that of the O. Use of a priori knowledge about the anatomy of the structures of interest would help alleviate that issue.

Conclusions

In this paper we proposed a 3-D histological volumes reconstruction approach, where smoothness is used to drive the reconstruction itself, in the absence of any external reference. Our method uses a modified version of the min–max curvature flow applied to surfaces extracted from an initial global rigid reconstruction of the input histological slices. A displacement field is obtained from the flow, which enables a flexible range of transformation spaces to be estimated and applied to each slice.

Our method is best suited for histological sections in which boundaries of interest are sufficiently contrasted to be extracted (either automatically or manually). Inevitably, some anatomical structures will present curved boundaries (e.g., the cortical foldings in the human brain). Here, we assume that the scale of the jaggedness along the cutting axis of the initially reconstructed boundaries is smaller than that of curved boundaries of the 3-D anatomical structures. Should that not be the case, a priori information about the anatomy of the structures could be provided to avoid smoothing these boundaries more than necessary.

We also proposed a quantitative smoothness measure, the Haralick contrast feature, based on co-occurrence matrices. Results confirm a strong correlation between a qualitative appraisal of the smoothness of the reconstructed volumes and the quantitative values of the contrast measures extracted from a narrow-band in a neighborhood around boundaries of interest. We note that since co-occurrence matrices may be computationally expensive, an alternative approach based on a binary segmentation of the gray-level volume could be used instead. This would considerably reduce the size of the matrices while still preserving the coarse/smooth aspect of the reconstructed volume.

Acknowledgments

This research is funded by the European Commission Fp6 Marie Curie Action Programme (MEST-CT-2005-021170). We are thankful to Dr. Tony Pridmore and the reviewers for their helpful comments and suggestions.

Appendix A. Co-occurrence matrices

Haralick et al. (1973) give the definition of GLCM for a 2-D image. The corresponding GLCMs for a 3-D volume of size $N_y \times N_x \times N_z$ follow straightforward. The lattice giving the spatial coordinates of the voxels is defined as $L=L_y \times L_x \times L_z$, with $L_y=\{1,2,\ldots,N_y\}$, $L_x=\{1,2,\ldots,N_x\}$ and $L_z=\{1,2,\ldots,N_z\}$. For N_g distinct gray levels, we define the intensity domain of a 3-D reconstructed volume as $G=\{0,1,\ldots,N_g-1\}$ and therefore, the volume can be specified by $I: L \mapsto G$. Its corresponding GLCM $P \in \mathcal{M}_{N_g \times N_g}$, computed along the angular directions α (in the (x, y) plane defined by the histological slices), θ (with respect to the z axis) and for distance between voxels d is :

$$\begin{aligned} P(i,j)_{d,\alpha,\theta} = Card\{&((k,l,m),(n,o,p) \in L \times L| \\ &I(k,l,m)=i, I(n,o,p)=j, \\ &\Delta((k,l,m),(n,o,p))=d, \\ &\angle((k,l),(n,o),x)=\alpha \\ &\angle((k,l,m),(n,o,p),z)=\theta\} \end{aligned} \tag{A.1}$$

These matrices are normalized by the number of pairs of voxels involved in their computation:

$$p(i,j) = \frac{1}{\sum P(i,j)} P(i,j) \tag{A.2}$$

The marginal probability matrices are:

$$p_x(j) = \sum_{i=0}^{N-1} p(i,j), \quad j=\{0,1,\ldots,N-1\} \tag{A.3}$$

$$p_y(i) = \sum_{j=0}^{N-1} p(i,j), \quad i=\{0,1,\ldots,N-1\} \tag{A.4}$$

Their corresponding mean and standard deviations are denoted here by μ_x, μ_y, σ_x, σ_y.

The textural features considered here are the following:

- Angular Second Moment (ASM):

$$f_1 = \sum_i \sum_j p(i,j)^2 \tag{A.5}$$

- Contrast:

$$f_2 = \sum_{i-j=0}^{N-1} (i-j)^2 \left(\sum_{i=0}^{N-1} \sum_{j=0}^{N-1} p(i,j) \right) \tag{A.6}$$

- Correlation:

$$f_3 = \frac{\sum_i \sum_j \left(i-\mu_y\right)(j-\mu_x)p(i,j)}{\sigma_y \sigma_x} \tag{A.7}$$

- Entropy:

$$f_9 = -\sum_i \sum_j p(i,j) log(p(i,j)) \tag{A.8}$$

• Difference variance

$$f_{10} = \sum_{i=0}^{N_g-1} (i-f_{11})^2 p_{x-y}(i) \tag{A.9}$$

$$p_{x-y}(k) = \sum_i \sum_j p(i,j), \quad k = |i-j| \tag{A.10}$$

$$f_{11} = -\sum_{i=0}^{N_g-1} p_{x-y}(i) log\left(p_{x-y}(i)\right) \tag{A.11}$$

• Information measure of correlation f_{12}

$$f_{12} = \frac{f_9 - \left(-\sum_i \sum_j p(i,j) log\left(p_x(j) p_y(i)\right)\right.}{\max\left\{-\sum_j p_x(j) log p_x(j), -\sum_i p_y(i) log p_y(i)\right\}} \tag{A.12}$$

References

Baheerathan, S., Albregtsen, F., Danielsen, H., 1998. Registration of serial sections of mouse liver cell nuclei. J. Microsc. 192 (1), 37–53.

Bardinet, E., Ourselin, S., Dormont, D., Malandain, G., Tandé, D., Parain, K., Ayache, N., Yelnik, J., 2002. Co-registration of histological, optical and MR data of the human brain. MICCAI, 1, pp. 548–555.

Breen, M.S., Lazebnik, R.S., Wilson, D.L., 2005. Three-dimensional registration of magnetic resonance image data to histological sections with model-based evaluation. Ann. Biomed. Eng. 33 (13), 1100–1112.

Braumann, U., Kuska, J.P., Einenkel, J., Horn, L.C., Löffler, M., Höckel, M., 2005. Three-dimensional reconstruction and quantification of cervical carcinoma invasion fronts from histological serial sections. IEEE Trans. Med. Imaging 24 (10), 1286–1307.

Chakravarty, M.M., Bedell, B.J., Zehntner, S.P., Evans, A.C., Collins, D.L., 2008. Three-dimensional reconstruction of serial histological mouse brain sections. ISBI, pp. 987–990.

Chakravarty, M.M., Bertrand, G., Hodge, C.P., Sadikot, A.F., Collins, D.L., 2006. The creation of a brain atlas for image guided neurosurgery using serial histological data. Neuroimage 30 (2), 359–376.

Cifor, A., Pridmore, T., Pitiot, A., 2009. Smooth 3-D reconstruction for 2-D histological images. IPMI. Vol. 5636 of LNCS, pp. 350–361. Springer.

Cohen, F., Yang, Z., Huang, Z., Nissanov, J., 1998. Automatic matching of homologous histological sections. IEEE Trans. Biomed. Eng. 445 (5), 642–649.

Dauguet, J., Delzescaux, T., Condé, F., Mangin, J.-F., Ayache, N., Hantraye, P., Frouin, V., 2007. Three-dimensional reconstruction of stained histological slices and 3D non-linear registration with in-vivo MRI for whole baboon brain. J. Neurosci. Meth. 164, 191–204.

Dauguet, J., Mangin, J.-F., Delzescaux, T., Frouin, V., 2004. Robust inter-slice intensity normalization using histogram scale-space analysis. MICCAI (1), pp. 242–249.

Deverell, M., Salisbury, J., Cookson, M., Holman, J., Dykes, E., Whimster, F., 1993. Three-dimensional reconstruction: methods of improving image registration and interpretation. Anal. Cell. Pathol. 5, 253–263.

Dice, L.R., 1945. Measures of the amount of ecologic association between species. Ecology 26 (3), 297–302.

Gefen, S., Tretiak, O., Nissanov, J., 2003. Elastic 3D alignment of rat brain histological images. IEEE Trans. Med. Imaging 22 (11), 1480–1489.

Goldszal, A., Tretiak, O., Hand, P., Bhasin, S., McEachro, D., 1995. Three-dimensional reconstruction of activated columns from 2-[14c]deoxy-d-glucose data. Neuroimage 2 (1), 9–10.

Goldszal, A., Tretiak, O., Liu, D., Hand, P., 1996. Multimodality multidimensional image analysis of cortical and subcortical plasticity in the rat brain. Ann. Biomed. Eng. 24 (3), 430–439.

Gomes, J., Faugeras, O.D., 2000. Level sets and distance functions. ECCV (1), pp. 588–602.

Gotlieb, C.C., Kreyszig, H.E., 1990. Texture descriptors based on co-occurrence matrices. Comput. Vis. Graph Image Proc. 51 (1), 70–86.

Guest, E., Baldock, R., 1995. Automatic reconstruction of serial sections using the finite element method. Bioimaging 3, 154–167.

Guest, E., Berry, E., Baldock, R.A., Fidrich, M., Smith, M.A., 2001. Robust point correspondence applied to two- and three-dimensional image registration. IEEE Trans. Pattern Anal. Mach. Intell. 23 (2), 165–179.

Haralick, R.M., Shanmugam, K., Dinstein, I., 1973. Textural features for image classification. IEEE Trans. Syst. Man Cybern. 3 (6), 610–621.

Humm, J., Macklis, R., Lu, X., Yang, Y., Bump, K., Beresford, B., Chin, L., 1995. The spatial accuracy of cellular dose estimates obtained from 3D reconstructed serial tissue autoradiographs. Phys. Med. Biol. 40 (18), 163–180.

Ju, T., Warren, J., Carson, J., Bello, M., Kakadiaris, I., Chiu, W., Thaller, C., Eichele, G., 2006. 3D volume reconstruction of a mouse brain from histological sections using warp filtering. J. Neurosci. Meth. 156, 84–100.

Kim, B., Boes, J., Frey, K., Meyer, C., 1997. Mutual information for automated unwarping of rat brain autoradiographs. Neuroimage 5 (1), 31–40.

Kim, B., Frey, K.A., Mukhopadhayay, S., Ross, B.D., Meyer, C.R., 1995. Co-registration of MRI and autoradiography of rat brain in three-dimensions following automatic reconstruction of 2D data set. CVRM. Vol. 905 of LNCS. Springer, pp. 262–266.

Krinidis, S., Nikou, C., Pitas, I., 2002. 3D volume reconstruction by serially acquired 2D slices using a distance transform-based global cost function. SETN, pp. 390–400.

Laissue, P., Kenwright, C., Hojjat, A., Colchester, A.C.F., 2008. Using curve-fitting of curvilinear features for assessing registration of clinical neuropathology with in vivo mri. MICCAI (2), pp. 1050–1057.

Malandain, G., Bardinet, E., 2003. Intensity compensation within series of images. MICCAI (2), pp. 41–49.

Malandain, G., Bardinet, E., Nelissen, K., Vanduffel, W., 2004. Fusion of autoradiographs with an MR volume using 2-D and 3-D linear transformations. Neuroimage 23 (1), 111–127.

Malladi, R., Sethian, J.A., 1996. Flows under min/max curvature flow and mean curvature: applications in image processing. ECCV. Springer-Verlag, pp. 251–262.

Malladi, R., Sethian, J.A., 1997. Level set methods for curvature flow, image enhancement, and shape recovery in medical images. Proc. Conf. Visualization and Mathematics. Springer-Verlag, pp. 329–345.

Mega, M., Chen, S., Thompson, P., Woods, R., Karaca, T., Tiwari, A., Vinters, H., Small, G., Toga, A., 1997. Mapping histology to metabolism: coregistration of stained whole-brain sections to premortem pet in Alzheimer's disease. Neuroimage 5 (7), 147–153.

Osher, S., Sethian, J.A., 1988. Fronts propagating with curvature-dependent speed: algorithms based on Hamilton–Jacobi formulations. J. Comput. Phys. 79, 12–49.

Osher, S.J., Fedkiw, R.P., 2002. Level Set Methods and Dynamic Implicit Surfaces. Springer.

Ourselin, S., Bardinet, E., Dormont, D., Malandain, G., Roche, A., Ayache, N., Tande, D., Parain, K., Yelnik, J., 2001a. Fusion of histological sections and MR images: towards the construction of an atlas of the human basal ganglia. MICCAI. Vol. 2208 of LNCS, pp. 743–751.

Ourselin, S., Roche, A., Prima, S., Ayache, N., 2000. Block matching: a general framework to improve robustness of rigid registration of medical images. MICCAI. Vol. 1935 of LNCS. Springer, pp. 557–566.

Ourselin, S., Roche, A., Subsol, G., Pennec, X., Ayache, N., 2001b. Reconstructing a 3D structure from serial histological sections. Image Vis. Comput. 19 (1–2), 25–31.

Pitiot, A., Guimond, A., 2008. Geometrical regularization of displacement fields for histological image registration. MedIA 12 (1), 16–25.

Pitiot, A., Pausova, Z., Prior, M., Perrin, J., Loyse, N., Paus, T., 2007. Magnetic resonance imaging as a tool for in vivo and ex vivo anatomical phenotyping in experimental genetic models. Hum. Brain Mapp. 28, 555–566.

Rousseeuw, P.J., 1984. Least median of squares regression. J. Am. Stat. Assoc. 79 (388), 871–880.

Schmitt, O., Modersitzki, J., Heldmann, S., Wirtz, S., Fischer, B., 2007. Image registration of sectioned brains. Int. J. Comput. Vision 73 (1), 5–39.

Schormann, T., Zilles, K., 1997. Limitations of the principal-axes theory. Med. Imaging IEEE Trans. 16 (6), 942–947.

Simonetti, A.W., Elezi, V.A., Farion, R., Malandain, G., Segebarth, C., Rémy, C., Barbier, E.L., 2006. A low temperature embedding and section registration strategy for 3D image reconstruction of the rat brain from autoradiographic sections. J. Neurosci. Meth. 158 (2), 242–250.

Streicher, J., Weninger, W.J., Müller, G.B., 1997. External marker-based automatic congruencing: a new method of 3D reconstruction from serial sections. Anat. Rec. 248, 583–602.

Tan, Y., Hua, J., Dong, M., 2007. Feature curve-guided volume reconstruction from 2D images. ISBI, pp. 716–719.

Thompson, P., Toga, A.W., 1996. A surface-based technique for warping 3-dimensional images of the brain. IEEE Trans. Med. Imaging 15, 402–417.

Timsari, B., Tocco, G., Bouteiller, J., Baudry, M., Leahy, R., 1999. Accurate registration of auto radiographic images of rat brain using a 3-D atlas. International Conference on Imaging Science Systems and Technology.

Toga, A., Goldkorn, A., Ambach, K., Chao, K., Quinn, B., Yao, P., 1997. Postmortem cryosectioning as an anatomic reference for human brain mapping. Comput. Med. Imaging Graph. 21 (11), 131–141.

Wirtz, S., Fischer, B., Modersitzki, J., Schmitt, O., 2004. Super-fast elastic registration of histologic images of a whole rat brain for three-dimensional reconstruction. SPIE Med. Imaging, Vol. 5730, pp. 14–19.

Yelnik, J., Bardinet, E., Dormont, D., Malandain, G., Ourselin, S., Tand, D., Karachi, C., Ayache, N., Cornu, P., Agid, Y., 2007. A three-dimensional, histological and deformable atlas of the human basal ganglia. I. Atlas construction based on immunohistochemical and MRI data. Neuroimage 34 (2), 618–638.

Yushkevich, P.A., Avants, B.B., Ng, L., Hawrylycz, M., Burstein, P.D., Zhang, H., Gee, J.C., 2006. 3D mouse brain reconstruction from histology using a coarse-to-fine approach. WBIR. Vol. 4057 of LNCS. Springer, pp. 230–237.

Zhao, R., Gabriel, M., Belford, G.G., 2004. An extendable registration similarity metric for anatomical image sequence alignment. ISBI, pp. 736–739.

Zhao, W., Young, T., Ginsberg, M., 1993. Registration and three-dimensional reconstruction of autoradiographic images by the disparity analysis method. IEEE Trans. Med. Imaging 12 (4), 782–791.